Dynamic analysis of aeroacoustic hysteresis of a low-Reynolds-number airfoil

Wangqiao Chen
State Key Laboratory of Turbulence and Complex Systems, Aeronautics and Astronautics, College of Engineering, Peking University, Beijing 999077, People's Republic Of China

Hanbo Jiang*
Eastern Institute for Advanced Study, Yongriver Institute of Technology, Ningbo 315000, People's Republic Of China

Xun Huang
State Key Laboratory of Turbulence and Complex Systems, Aeronautics and Astronautics, College of Engineering, Peking University, Beijing 100871, People's Republic Of China

(Received 9 January 2022; accepted 15 September 2022; published 26 September 2022)

Lifting surfaces in aerospace and power industry applications produce tonal noise at low-to-medium Reynolds number, significantly contributing to global noise annoyance. The dominant noise frequency depends on the freestream velocity, angle of attack, and surrounding environment. This work reports that the frequency spectra can exhibit different behavior at the same flow condition, which constitutes the hysteresis phenomenon. Time-resolved particle image velocimetry (PIV) of boundary-layer flows near the trailing edge and far-field noise measurements are performed simultaneously and synchronously. Two branches of experiments are conducted with the freestream velocity increasing and decreasing, respectively. Results are analyzed from the perspective of modern dynamical systems. The boundary layer is viewed as the forced oscillator, with the acoustic waves being the forcing mechanism. Both the bifurcation theory and the Poincaré section are introduced to investigate the dynamic process when freestream velocity changes. Typically, the dominant frequency of acoustic waves matches that of the most amplified disturbances in the boundary layer, which is consistent with existing literature on the same noise generation mechanism. However, dual peaks can be observed at specific freestream velocities: one matches the natural frequency of the current flow state while the other matches that of the previous state. The associated transitions between periodic and quasiperiodic oscillations constitute the hysteresis phenomenon.

DOI: 10.1103/PhysRevFluids.7.094401

I. INTRODUCTION

The mechanism behind airfoil tonal noise generation is still an open question in the aeroacoustic community. Research on the discrete tones from isolated airfoils dates back to the work of Paterson *et al.* [1], who argued that these tones were related to vortex shedding similar to aeolian tones generated by bluff bodies. Later, Arbey and Bataille [2] showed that the measurements agreed well with the linear stability theory regarding the frequency of the most significant tone. An acoustic feedback loop was identified in the pioneering studies [2,3], which states that boundary-layer insta-

*hanbojiang@eias.ac.cn

 ©2022 American Physical Society

bility waves are scattered into acoustic waves [4] at the trailing edge and the upstream-propagating acoustic waves reinforce the instability waves at the maximum velocity point [5,6].

This feedback loop can be viewed as the resonance between the boundary-layer flow and the acoustic waves. Therefore, it can be analyzed with modern dynamical systems theory [7,8]. Instead of finding precise solutions to the physical problem, the theory qualitatively describes the steady state of a given dynamical system or transitions between these states. For instance, Rowley and Williams [9] employed the dynamical systems theory to study the resonance problem of flow over a cavity, gaining insight into the mechanisms by which open-loop control can affect flow features. The work of Rowley and Williams [9] is of particular relevance, as the discrete tones from the airfoil trailing edge are similarly ascribed to resonance mechanisms, thus motivating the present study.

Without loss of generality, the laminar boundary layer can be viewed as a nonlinear dynamical system with the acoustic waves acting as an external force. The natural frequency of the system f_n matching that of the most amplified disturbances can be obtained by numerically solving the Orr-Sommerfeld equation [2,10]. The frequency of the external forcing f_e can be measured directly by microphone. Typically, f_n matches f_e when the feedback loop is established [2,11,12]. The existing acoustic-feedback theories [2,3] are based on a self-excited noise-generation mechanism, implying that the frequency of dominant tones is chosen by the physical system (flow, airfoil, and wind tunnel) alone. One important feature of self-sustained oscillators is that these oscillations cannot be easily affected by different initial conditions [7]. Hysteresis is a property of path-dependent dynamic systems. The solution of a hysteresis system depends on how the state variable changed in the past, and two solutions can exist for the same condition. For instance, Sanmiguel-Rojas and Mullin [13] observed a hysteresis loop when investigating transitional flows in a pipe with sudden expansion. A subsequent work of Nguyen *et al.* [14] conducted two branches of simulations with the Reynolds number increasing from steady laminar flow and decreasing from a transitional unsteady state. Nguyen *et al.* [14] confirmed that two flow solutions can exist for the same Reynolds number, depending on the steps of Reynolds number and computation time. In aerodynamics, hysteresis was also studied during the stall process on two-dimensional airfoils, due to the difference between the separation angle and the reattachment angle [15]. Examples can also be found in cavity flow [9], airfoil separation bubble [16], and fluid phase transition studies [8], attracting great efforts in various research communities. Typically, systems with hysteresis are nonlinear and can be challenging to model precisely. A mathematical description of the hysteresis loop is beyond the scope of this introduction. Nevertheless, the dynamical systems theory can still gain qualitative properties of solutions from general principles. For instance, the Poincaré section can facilitate identifying whether the oscillation of a dynamical system is periodic or quasiperiodic, by tracing its state variables.

In this work, we find that the frequency of the dominant tone does not have to match that of the most amplified disturbances in the boundary layer. A dynamic lag can exist between f_n and f_e when the freestream velocity changes. The frequency spectra can exhibit different behavior at the same freestream velocity, depending on the freestream velocity increasing or decreasing. This phenomenon of hysteresis, which has not been reported elsewhere, constitutes one of the major findings in this work.

The remaining parts of this article are organized as follows. The experimental setup and phenomena are discussed in Sec. II to show the hysteresis in the trailing edge noise. Next, the boundary-layer instability and the forced synchronization oscillation system are discussed in Sec. III. The system states are also discussed by employing the Poincaré section in Sec. III A. Finally, Sec. IV concludes the present research.

II. EXPERIMENTAL MEASUREMENTS

Experiments were conducted in a closed-circuit low-turbulence wind tunnel with a 1 m × 1 m × 4 m test section at Peking University. Figure 1 shows the experimental setup. The boundaries of the test section were treated to minimize reflections. A 0.2 m chord NACA 0012 airfoil was

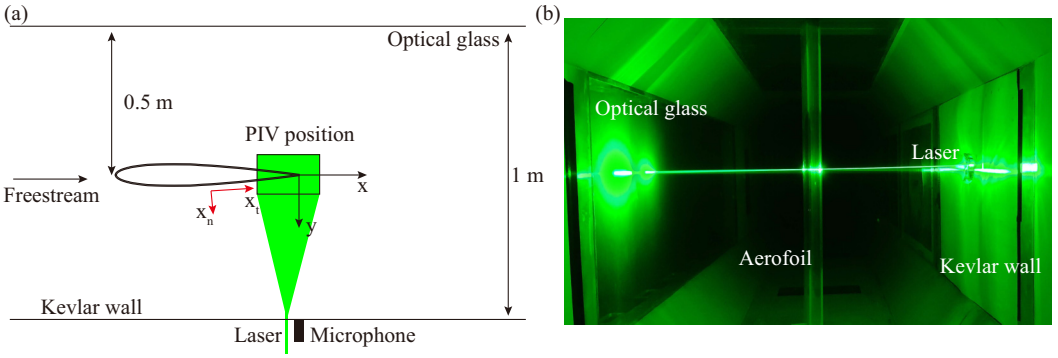

FIG. 1. (a) The experimental setup and (b) the photograph.

installed with a fixed angle of attack at 0 deg. The testing airfoil speed was from 11 m/s to 25 m/s with the corresponding chord-based Reynolds number from 1.4×10^5 to 3.3×10^5. The airfoil aerodynamic noise was measured by a BSWA-MA401 high-precision microphone that was flush mounted to the side wall of the test section. The microphone was further covered by a tensioned Kevlar 120 cloth (0.6 m × 1.2 m, only one side of the wind tunnel and smaller than the test section scales) to reject wind tunnel boundary-layer interference and permit the transmission of sound with little loss [17]. The sampling frequency was set to 50 kHz and the sound pressure level (SPL) results were acquired by averaging over 36 blocks (length 1×10^5, frequency resolution 0.5 Hz) for statistical convergence.

The time-resolved particle image velocimetry (PIV) technique was employed to capture velocity fluctuations inside the boundary layer. The injected seeding particles were first illuminated by a 1 mm thick double-pulsed DCQ-60 laser sheet and then visualized by a 1280 × 800 pixels Phantom-V2512 camera with 6 kHz acquisition frequency. Two coordinate systems were used in the experiments. One was originated at the trailing edge of the airfoil, with x aligned with the downstream direction and y normal to the chord. The other coordinate system was specifically designed for describing local boundary flow, with x_t and x_n tangent and normal to the airfoil surface, respectively. A National Instruments 24-bit PXI-4496 card was used to acquire samples from the microphone and the acquisition was synchronized to the high-speed camera.

Figure 2 shows the vortical structures on the velocity vectors at $u_\infty = 18.1$ m/s in (a) and (b) when the inlet speed increases, and in (c) and (d) when the inlet speed decreases. As shown in Figs. 2(a) and 2(c), the time-averaged flow field is essentially symmetrical with respect to the chord, since the angle of attack is fixed at 0 deg. Moreover, the instantaneous vorticity results in Figs. 2(b) and 2(d) show the gradual development of small flow fluctuations inside the boundary layer of the airfoil. The governing physics is often associated with the Tollmien-Schlichting (T-S) instability mechanism. Furthermore, the fluctuations on the top and bottom sides around the trailing edge are in-phase in Fig. 2(c) and out-of-phase in Fig. 2(d). This difference signifies that the system state has bifurcation at $u_\infty = 18.1$ m/s.

In this work, the PIV measurements were performed at velocities from $u_\infty = 17.7$ m/s to $u_\infty = 19.0$ m/s. The instantaneous vorticity contours are quite similar to those in Fig. 2 and are therefore omitted here for brevity. Figure 3 shows the tangential flow velocity profiles inside the boundary layer at −0.15 c, −0.1 c, −0.05 c, and 0 c. The tangential velocity results are normalized by the trailing edge velocity u_e, the symbol $\overline{(\cdot)}$ represents the arithmetic mean value, and the symbol δ^* indicates the displacement thickness of the boundary layer (the chord-based dimensionless profile results are shown in Supplemental Material [18]). The flow separated at the near wall region (especially at −0.15 c and −0.1 c). It can be seen that the normalized mean velocity profiles are almost identical at different mean flow speeds, whereas the velocity fluctuations gradually develop along the airfoil surface, which is governed by the growing T-S instability waves.

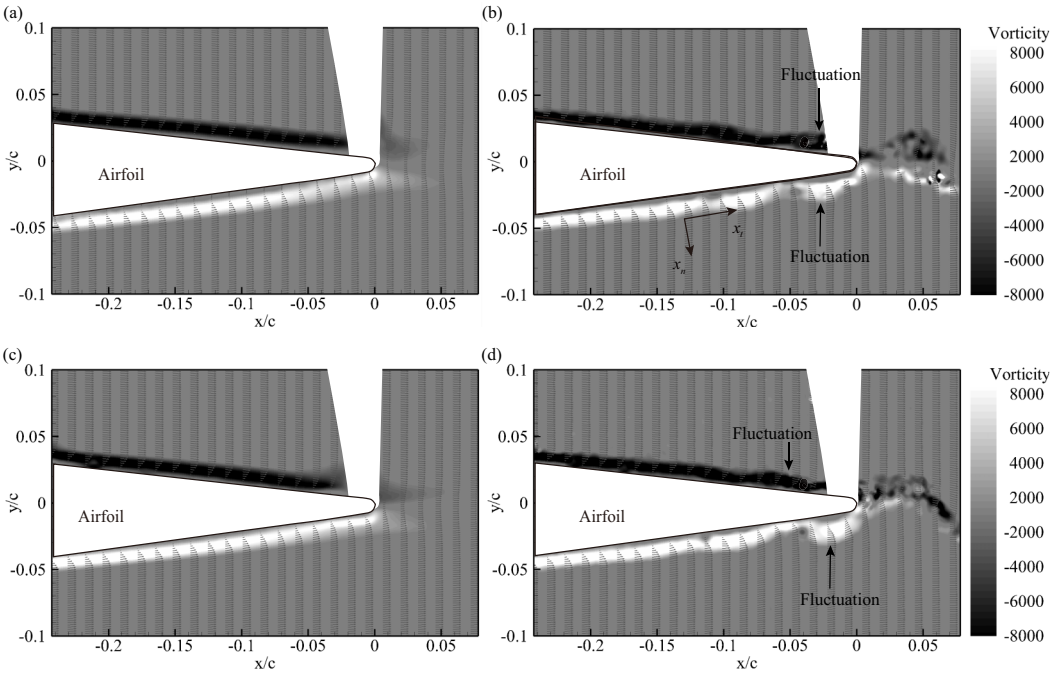

FIG. 2. Time-averaged and instantaneous contours of the spanwise vorticity at $u_\infty = 18.1\,\mathrm{m/s}$ for (a and b) increasing speed and (c and d) decreasing speed.

The classical hysteresis loops for low-Reynolds-number airfoils appear in aerodynamic loads during oscillatory motion with varying angle of attack [19]. In contrast, the hysteresis loop observed in this work concerns the dominant frequencies as a function of varying mean flow speeds, where u_∞ is first increased from 11 m/s to 25 m/s with a velocity step around $\Delta u_\infty = 0.23\,\mathrm{m/s}$ (5 rpm

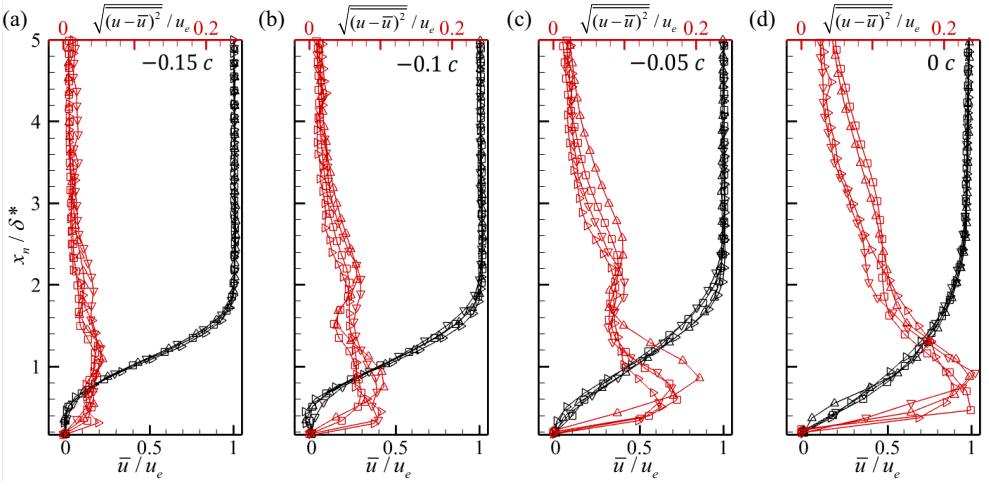

FIG. 3. Mean (black) and root mean square fluctuations (red) of the tangential velocity at different surface locations under various freestream velocities: □, $u_\infty = 17.7$ m/s; △, $u_\infty = 18.1(+)$ m/s; ▽, $u_\infty = 18.1(-)$ m/s; ▷, $u_\infty = 19.0$ m/s.

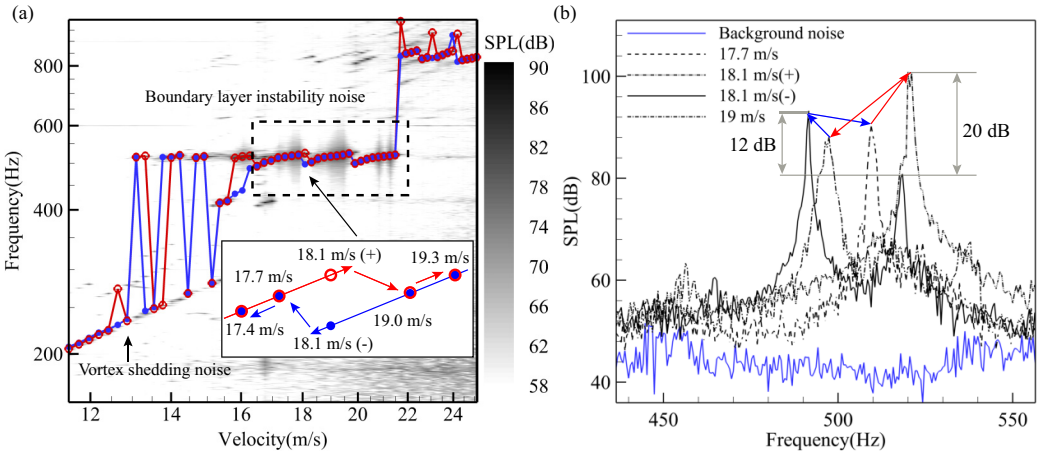

FIG. 4. The hysteresis loop of the dominant frequency, where (a) is the spectrum of the microphone signal at different mean flow speeds, and (b) shows the comparisons of the SPL values at the representative flow speeds inside the loop. The background noise is measured at $u_\infty = 18.0\,\mathrm{m/s}$.

difference of the driving system) and then modified backward to 11 m/s. During each aerodynamic and aeroacoustic measurement, the freestream velocity was kept constant for at least two minutes to ensure a steady aerodynamic state was achieved. The repeatability of the measurements was checked by performing the experiments consecutively three times.

Figure 4(a) shows the spectrum of the microphone signal with respect to the mean flow speeds. The focus of this research is on the noise induced by the T-S instability waves at the frequency range between 400 Hz and 600 Hz. The enlarged inset in Fig. 4(a) clearly shows a hysteresis cycle, where the direction of the arrows represents the flow speed modification setups during the tests. The good agreement between the ($\circ$) cycle and the ($\cdot$) cycle at $u_\infty = 17.4\mathrm{m/s}$, 17.7 m/s, 19.0 m/s, and 19.3 m/s suggests remarkable accuracy of the measurements. However, differences are also visible at specific freestream velocities such as 14 m/s, 16 m/s, 18 m/s, etc., producing several loops of hysteresis.

When comparing two branches of experiments, it is notable that the frequency values are mainly composed of three regimes: (i) the dominant frequency increased linearly with the freestream velocity for $u_\infty \leqslant 16\,\mathrm{m/s}$ ($\mathrm{Re} \leqslant 2 \times 10^5$); (ii) the frequency varied within a small range centered approximately at 500 Hz when $16\,\mathrm{m/s} < u_\infty \leqslant 22\,\mathrm{m/s}$ ($2 \times 10^5 < \mathrm{Re} \leqslant 2.9 \times 10^5$); and (iii) the frequency values were around 800 Hz over $22\,\mathrm{m/s} < u_\infty \leqslant 25\,\mathrm{m/s}$ ($2.9 \times 10^5 < \mathrm{Re} \leqslant 3.3 \times 10^5$). Interestingly, the hysteresis phenomenon was found in all the above regions, despite the associated noise generation mechanisms being different. In region (i), the dominant noise was ascribed to laminar-boundary-layer vortex shedding at the trailing edge as arrowed in Fig. 4(a). The correspondence between the flow structure and acoustic emissions was confirmed by PIV and noise measurements [10,20,21]. In regions (ii) and (iii), the T-S wave diffraction contributed to the tonal noise emission, as shown in the following section. However, in region (iii), separation bubbles near the trailing edge also generated discrete tones [12]. Moreover, as the velocity (Reynolds number) increased, the separation bubbles disappeared. The laminar boundary layer transited into a turbulent boundary layer at high Reynolds number, and the broadband noise was dominant [22]. In other words, different noise generation mechanisms co-existed and thus were challenging to analyze. Therefore, we focused on the small hysteresis loop around $u_\infty = 18\,\mathrm{m/s}$, where the scattering of T-S waves dominated the tonal noise generation. A closer view of the hysteresis loop was plotted over a small freestream velocity range, $16\,\mathrm{m/s} < u_\infty < 20\,\mathrm{m/s}$, where the directions of the change in u_∞ are also indicated by arrows.

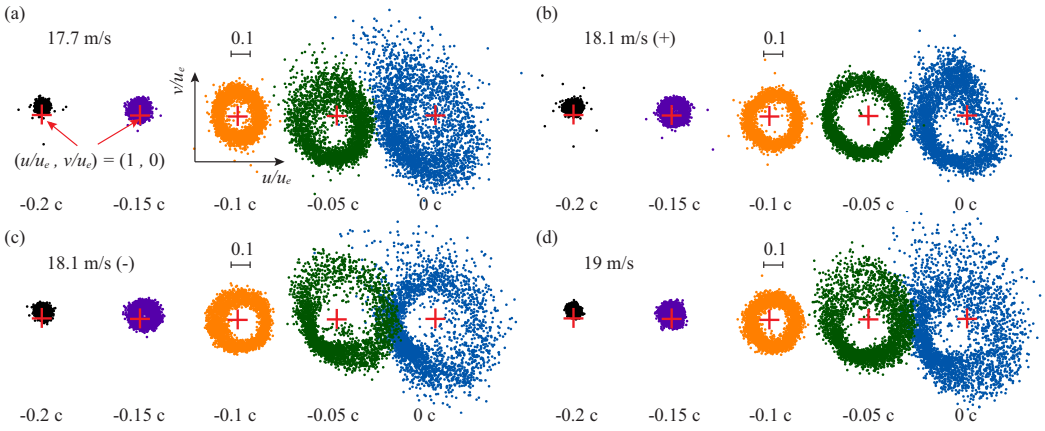

FIG. 5. Stabilized modes and destabilization at different boundary-layer locations and flow speeds. Projections of the phase portraits on the plane $(u/u_e, v/u_e)$.

The inset of Fig. 4(a) shows that the hysteresis loop consists of a positive half-cycle, where u_∞ is increased from 17.7 m/s to 19.4 m/s, and a negative half-cycle, where u_∞ is decreased from 19.0 m/s backward to 17.4 m/s. Figure 4(b) shows the corresponding SPL results at two representative flow speeds, where the blue and red arrows indicate the shiftings of the dominant frequencies inside the positive half-cycle and negative half-cycle, respectively. At first, the dominant frequency increases with the freestream velocity changing from 17.7 m/s to 18.1 m/s and suddenly drops at $u_\infty = 19.0$ m/s. After that, the dominant frequency decreases with the freestream velocity changing from 19.0 m/s to 18.1 m/s and suddenly increases at $u_\infty = 17.7$ m/s. It should be noted that results of 18.1 m/s in both branches exhibited similar dominant frequencies (517 Hz and 520 Hz), but with a difference of 20 dB in the peak values. More importantly, in the u_∞ decreasing process, dual peaks occurred at 18.1 m/s. A similar observation was also reported by Paterson *et al.* [1]. As discussed later, one peak is the frequency of the external forcing (acoustic waves) f_e, and the other is the system's natural frequency f_n (that of the most amplified disturbances). Moreover, in Fig. 4(b), the strength of the tonal noise at $u_\infty = 18.1$ m/s(+) is about 100 dB, which is much larger than the results from acoustically treated wind tunnels, wherein the tonal noise strength almost distributed from 60 to 80 dB [1,2,10,20,21]. The hard wall of the wind tunnel may be the reason for the high-value SPL results. In this work, the Kevlar cloth is only covered on one side of the wind tunnel. The acoustic environment provided by the other walls allows the wind tunnel to follow hard-wall acoustic conditions. Compared with the low-strength SPL results from acoustically treated wind tunnels, Nash *et al.* [12] measured the high-value tonal noise at 26 m/s and reported that the tonal noise is up to 40 dB above the broadband noise [same in Fig. 4(b)] in a hard-wall wind tunnel. This feature can also be found in the spectrum results from Plogmann *et al.* [5]. Furthermore, Pröbsting *et al.* [21] documented that the trailing edge noise was strongest at zero angle of attack, which may be another reason for the high-value SPL results in Fig. 4(b). It should be mentioned that the frequency resolution also affects the amplitude in the spectrum. In this work, different frequency resolutions may result in a difference of up to 5 dB. For example, the strength of the tonal noise at $u_\infty = 18.1$ m/s(+) is about 100 dB with 0.5 Hz frequency resolution [as shown in Fig. 4(b)], 104 dB with 2 Hz frequency resolution, and 105 dB with 5 Hz frequency resolution. The comparison results are attached in Supplemental Material [18].

III. HYSTERESIS MECHANISM

Figures 5(a)–5(d) illustrate the evolution of stroboscopic sections at different wall-tangential locations (the same wall-normal distance, $x_n = 0.02$ c, which is the boundary-layer thickness at

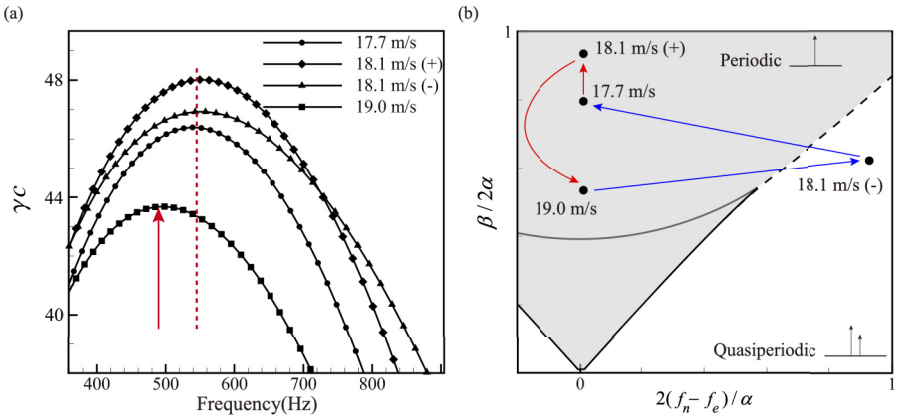

FIG. 6. The natural frequency at different speeds, where (a) is the spatial growth rate from Fig. 3(a) and 3(b) is the synchronization tongue for the forced van der Pol oscillator.

$x_t = -0.2c$ and $u_\infty = 17.7\,\mathrm{m/s}$) for all flow speeds. The horizontal and vertical axes indicate normalized wall-tangential and wall-normal velocity components. The red cross denotes a reference state of $(u_t/u_e, u_n/u_e) = (1, 0)$. For all flow speeds presented, the phase portraits are distributed around the reference state, demonstrating the phase coherence between velocity disturbances. The distance between each point and the reference state measures the magnitude of local velocity disturbances. These points are expected to exhibit ideal point or circular patterns for harmonic oscillations. Here we introduce the bounding circle, the smallest circle containing all of the points at each location. In Figs. 5(a)–5(d), the radius of the bounding circle increases from $x_t = -0.2\,\mathrm{c}$ to $x_t = 0\,\mathrm{c}$, suggesting that the instability waves gradually develop along the wall-tangential direction. In detail, the boundary layer is stable before $x_t = -0.15\,\mathrm{c}$, and the fluctuation increases rapidly after this location. It should be noted that the regularity of the point distributions becomes worse towards the trailing edge, i.e., $x_t = -0.05\,\mathrm{c}$ and $x_t = 0\,\mathrm{c}$, meaning the destabilization of the boundary-layer flow. Therefore, we chose the location $x_t = -0.15\,\mathrm{c}$ for the following discussion to ensure that the linear stability analysis is applicable. Moreover, the linear stability analysis results around $x_t = -0.15\,\mathrm{c}$ are attached in Supplemental Material [18]. The spatial growth rate achieves the maximum value at $x_t = -0.15\,\mathrm{c}$ at every wind speed, and the conclusions will not change if velocity profiles are taken at a slightly upstream and downstream position.

Figure 6(a) shows the spatial growth rate [$\gamma(\mathrm{m}^{-1})$, dimensionless with the chord of airfoil] at $x_t = -0.15\,\mathrm{c}$, which was obtained by performing a spatial linear stability analysis with the mean velocity profiles from Fig. 3(a) (at $x_t = -0.15\,\mathrm{c}$). In linear stability analysis, the mean velocity profiles are interpolated using the inverse ratio function $(1/x_n)$ to ensure a better resolution. The maximum growth rate at $u_\infty = 18.1\,\mathrm{m/s}$ is larger than that at the remaining conditions, which may be related to the amplitude of the tonal noise in Fig. 4(d). The frequency at which the maximum growth rate occurs is the system's natural frequency f_n. It is found that the natural frequency f_n at $u_\infty = 17.7\,\mathrm{m/s}$ is close to those at $u_\infty = 18.1\,\mathrm{m/s}$ for both increasing and decreasing processes. These peaks are all around 520 Hz, matching those associated natural frequencies. On the other hand, when $u_\infty = 19.0\,\mathrm{m/s}$, the natural frequency f_n is approximately 30 Hz lower, and the maximum growth rate is also visibly lower than those at the other conditions. This finding implies that the flow state in the boundary layer changes suddenly, leading to a sharp drop of the dominant frequency around $u_\infty = 18.1\,\mathrm{m/s}$ in Fig. 4(a).

Nevertheless, two facts in Fig. 4 have yet to be explained by existing feedback loop theories: (i) only $u_\infty = 18.1(-)\,\mathrm{m/s}$ of the decreasing branch produced dual tones with a 12 dB difference in the peak values, while the other cases generated just a single tone; and (ii) at $u_\infty = 18.1(-)\,\mathrm{m/s}$,

the weak tone is close to the associated natural frequency while the strong tone is close to the natural frequency at $u_\infty = 19.0\,\mathrm{m/s}$, which was the previous flow state. These phenomena, however, can be easily understood with the help of a van der Pol oscillator (a typical dynamical system),

$$\frac{d^2g}{dt^2} + \alpha(g^2 - 1)\frac{dg}{dt} + \omega_0^2 g = \beta f(t), \tag{1}$$

where α and β are parameters of damping and forcing strength, g denotes the displacement, and $f(t)$ is the forcing function [7–9]. Without loss of generality, the system (1) is assumed to be forced harmonically. The van der Pol oscillation system was employed to analyze the system states in cavity noise problems [9]. Qualitatively, a forced oscillator can exhibit two states, periodic and quasiperiodic oscillations [8], depending on both f_n and f_e. When the frequency of external stimulus is sufficiently close to the natural frequency, meaning that f_e reaches f_n, the system (1) demonstrates periodic oscillations and the spectrum contains just a single peak [7]. When a difference exists between f_n and f_e, the quasiperiodic oscillation occurs and multiple peaks can be found in the spectrum.

Figure 6(b) shows a bifurcation diagram of the van der Pol oscillator, where $(f_n - f_e)/\alpha$ denotes the forcing frequency and $\beta/2\alpha$ represents the forcing amplitude. The solid and dashed lines denote the saddle-node bifurcation and the Andronov-Hopf bifurcation, respectively [7,23]. The definition of these bifurcations are shown in Supplemental Material [18]. The gray area shows periodic oscillation with only one tonal frequency at forcing frequency, and another area denotes the quasiperiodic oscillations with multiple peak frequencies. In the quasiperiodic region, the system states around the saddle-node bifurcation and Andronov-Hopf bifurcation are different [7]. The peak associated with natural dynamics can be concluded with two different features: (a) moves to coincide with forcing frequency (crossing the saddle-node bifurcation), and (b) is stable but becomes smaller and finally vanishes (crossing the Andronov-Hopf bifurcation). In this work, only the second process can be noticed [at 18.1 m/s(-)]. Therefore, results of $u_\infty = 17.7\,\mathrm{m/s}$, 19.1 m/s, and 18.1 m/s in the increasing process are periodic oscillations. This implies a frequency (phase) synchronization of oscillations by external forcing, in which the van der Pol oscillator (1) achieves a single solution. As a result, the oscillations are strictly periodic and synchronous with the forcing, and a single peak is at the frequency of forcing. In contrast, $u_\infty = 18.1\,\mathrm{m/s}$ in the decreasing process leads to a quasiperiodic oscillation and is close to the Andronov-Hopf bifurcation [7,8]. Two distinct peaks, namely, f_e and f_n, coexist as indicated by Fig. 6(b), indicating the absence of synchronization between the oscillating system and the forcing. Note that $u_\infty = 18.1\,\mathrm{m/s}$ of the increasing process produces the maximum forcing amplitude among the four states marked in Fig. 6(b), while $u_\infty = 19.0$ produces the least.

Unlike conventional forced oscillators, the natural frequency f_n varies first instead of the forcing frequency f_e in the present problem, although the latter f_e is affected accordingly by the former f_n. The varying processes in Fig. 6(b) can be described as follows: First, the oscillation at 17.7 m/s is periodic, and the forcing frequency is equal to the natural frequency. Next, when u_∞ increases from 17.7 m/s to 18.1 m/s, the natural frequency gradually grows with the freestream velocity. Then, the natural frequency f_n drops at some point after $u_\infty = 18.1\,\mathrm{m/s}$, as shown in Fig. 4(a). In the process, the forcing frequency subsequently changes following the natural frequency, and the system remains synchronized in a periodic oscillation. Therefore, the system remains in the gray area and the frequency difference $f_n - f_e$ is equal to zero, as shown in Fig. 6(b). Afterwards, in the u_∞ decreasing process (for example, from 20 m/s to 19.0 m/s), the natural and forcing frequencies decrease with the freestream velocity. The system remains stably synchronized during the u_∞ increasing process. However, when the freestream velocity u_∞ decreases from 19.0 m/s, a sudden jump of the natural frequency occurs as u_∞ decreases to $u_\infty = 18.1\,\mathrm{m/s}$, leading to a large frequency difference $f_n - f_e$. In the decreasing process, the peak at natural frequency is stable at 18.1 m/s(-) but becomes larger and finally dominant (as shown in Fig. 4), which denotes that the system at 18.1 m/s is close to the Andronov-Hopf bifurcation line in Fig. 6(b). In the experiments, the saddle-node bifurcation does not occur, which means the system states are above the solid line.

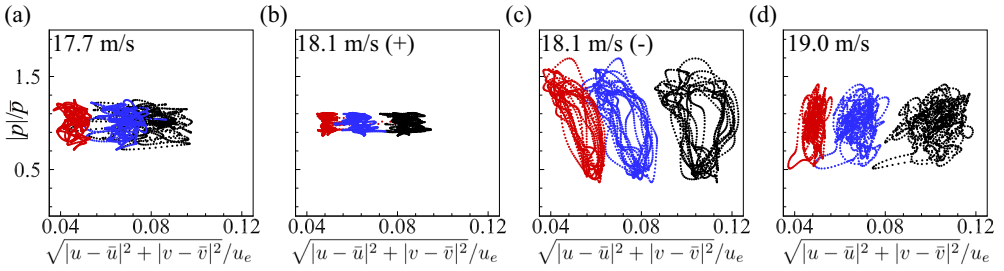

FIG. 7. Phase trajectories in the Poincaré sections at different locations, where $x_t = -0.1\,c$ (red), $-0.06\,c$ (blue), and $-0.02\,c$ (black), respectively.

Poincaré section analysis

The Poincaré section was initially proposed to study planetary orbits in the restricted three-body problem, which were too complicated to be explicitly describable. It is transversal to the state flow of the original system and is one dimension smaller than the original dynamical system. The Poincaré sections of periodic and quasiperiodic systems are related to a stable point and closed curves, respectively [7,8]. In the present problem, a fluid particle possesses three state variables: displacement, velocity, and acceleration (or force). To visualize the phase trajectory in the Poincaré section, we chose to fix the displacement at (x_t, x_n) and monitor the rest states. This implied that the distance between a fluid particle and the microphone would remain unchanged. The force acting on a fluid particle became equivalent to the acoustic pressures measured by the microphone because the associated acoustic phase delay was also time independent. Consequently, the Poincaré section comprised the local velocity disturbance and the acoustic pressure fluctuation, following the literature [24]. Three streamwise locations were selected with the same wall-normal distance, $x_n = 0.02\,c$. Figures 7(a)–7(d) present the associated phase trajectories in the Poincaré section at four states in the hysteresis loop. The three color points show results at $x_t = -0.1\,c$ (red), $-0.06\,c$ (blue), and $-0.02\,c$ (black), respectively. In Figs. 7(a), 7(b) and 7(d), the associated systems demonstrate periodic oscillations, and the trajectories in the Poincaré section should be a fixed point [7]. Different from the theoretical analysis, the results from measured data are inevitably disturbed by noise. Therefore, the trajectories in the Poincaré section represent scattered points randomly distributed in a certain range [as shown in Figs. 7(a), 7(b) and 7(d)]. Being distinct, the phase trajectories in Fig. 7(c) exhibit closed curves with large excursions, which indicates the existence of guiding manifolds of the resonant torus [7]. In this situation, there are multiple oscillation frequencies in the system, suggesting an absence of synchronization between the natural frequency and the forcing frequency. As a result, the system periodically switches between different states, producing quasiperiodic oscillations. Note that the Poincaré section for the location close to the trailing edge [see $x_t = 0.02\,\mathrm{c}$ in Fig. 7(c)] still successfully revealed the quasiperiodic oscillations, showing advantages over the phase-portrait analysis for the boundary-layer flow in Figs. 5(a)–5(d).

IV. SUMMARY

This work presents an experimental study of airfoil tonal noise generation at zero angle of attack, where we observed a hysteresis phenomenon in the frequency spectra. Both time-resolved PIV and acoustic measurements were employed to study the dynamical process of tonal noise emission and the associated flow evolution. Distinct tones, such as the vortex shedding noise and boundary-layer instability noise, were observed over a wide range of Reynolds numbers. The dominant tone demonstrated sudden jumps/drops at specific freestream velocities and did not always exhibit simple scaling.

The hysteresis phenomenon usually accompanies frequency jumps/drops and occurs almost universally. The hysteresis was found by conducting two branches of experiments with the freestream velocity increasing and decreasing, respectively. The dominant tone exhibited different behavior, depending on the increasing or decreasing freestream velocity. Several representative cases around a small hysteresis were presented with respect to the dynamical response of the tones in the spectrum. The experimentally acquired flow and noise data were analyzed from the perspective of modern dynamical systems. The boundary-layer flow was viewed as a forced oscillator, with the acoustic wave being the forcing. Concerning the relationship between forcing and natural frequencies, the nonlinear oscillator demonstrated periodic and quasiperiodic oscillations. The natural frequency suddenly changed at specific freestream velocities, inducing a large difference from the forcing frequency. In the freestream velocity increasing process, such a sudden change did not significantly affect oscillations because the forcing amplitude was sufficient to retain synchronization. Accordingly, only a single tone existed in the spectra. In contrast, when the freestream velocity decreased, the maximum growth rate in the boundary layer became lower than before. The acoustic forcing due to the diffraction of instability waves was subsequently weakened. The system lost synchronization and exhibited quasiperiodic oscillations, producing dual tones. To summarize, different noise spectra existed in the same flow conditions in the two branches, constituting the hysteresis phenomenon.

The bifurcation theory and the Poincaré section were introduced to describe transitions when freestream velocity changed. The associated qualitative analysis agreed well with typical features in the noise spectra. The successful application of modern dynamical systems implies that the associated control theory can be introduced for boundary-layer manipulation and noise reduction. Additionally, we wish to emphasize that although the present work only focuses on the boundary layer instability noise-dominated region, the hysteresis was also observed at other regimes, for example, $12\,\mathrm{m/s} < u_\infty \leqslant 16\,\mathrm{m/s}$, where the vortex shedding noise and the boundary-layer instability noise coexisted. This, however, will be left as a future topic.

ACKNOWLEDGMENTS

This work is partly supported by the National Science Foundation of China (Grant No. 91852201) and the Ministry of Industry and Information Technology of China (Grant No. MJ-2015-F-012-03). The authors would like to acknowledge Mr. J. M. Yu for his assistance with the PIV measurements.

[1] R. Paterson, P. Vogt, M. Fink, and C. Munch, Vortex noise of isolated airfoils, J. Aircraft **10**, 296 (1973).

[2] H. Arbey and J. Bataille, Noise generated by airfoil profiles placed in a uniform laminar flow, J. Fluid Mech. **134**, 33 (1983).

[3] C. Tam, Discrete tones of isolated airfoils, J. Acoust. Soc. Am. **55**, 1173 (1974).

[4] R. Amiet, Noise due to turbulent flow past a trailing edge, J. Sound Vib. **47**, 387 (1976).

[5] B. Plogmann, A. Herrig, and W. Würz, Experimental investigations of a trailing edge noise feedback mechanism on a NACA 0012 airfoil, Exp. Fluids **54**, 1480 (2013).

[6] S. Pröbsting and S. Yarusevych, Airfoil flow receptivity to simulated tonal noise emissions, Phys. Fluids **33**, 044106 (2021).

[7] A. Balanov, N. Janson, D. Postnov, and O. Sosnovtseva, *Synchronization: From Simple to Complex* (Springer, New York, 2000), p. 1.

[8] R. Abraham and Y. Ueda, *The Chaos Avant-garde: Memories of the Early Days of Chaos Theory*, World Scientific Series on Nonlinear Science: Monographs and Treatises (World Scientific, Singapore, 2000).

[9] C. Rowley and D. Williams, Dynamics and control of high-Reynolds-number flow over open cavities, Annu. Rev. Fluid Mech. **38**, 251 (2006).

[10] S. Pröbsting, J. Serpieri, and F. Scatano, Experimental investigations of aerofoil tonal noise generation, J. Fluid Mech. **747**, 656 (2014).

[11] A. McAlpine, E. Nash, and M. Lowson, On the generation of discrete frequency tones by the flow around an aerofoil, J. Sound Vib. **222**, 753 (1999).

[12] E. Nash, M. Lowson, and A. Mcalpine, Boundary-layer instability noise on aerofoils, J. Fluid Mech. **382**, 27 (1999).

[13] E. Sanmiguel-Rojas and T. Mullin, Finite-amplitude solutions in the flow through a sudden expansion in a circular pipe, J. Fluid Mech. **691**, 201 (2012).

[14] M. Q. Nguyen, M. S. Shadloo, A. Hadjadj, B. Lebon, and J. Peixinho, Perturbation threshold and hysteresis associated with the transition to turbulence in sudden expansion pipe flow, Int. J. Heat Fluid Flow **76**, 187 (2019).

[15] W. Morris, C. Zenker, J. Ingraham, and T. Wolfenbarger, A theory of stall hysteresis – Why the reattachment angle is less than the separation stall angle, in *AIAA Scitech 2020 Forum* (AIAA, 2020).

[16] Z. Yang, H. Igarashi, M. Martin, and H. Hu, An experimental investigation on aerodynamic hysteresis of a low-Reynolds number airfoil, in *46th AIAA Aerospace Sciences Meeting and Exhibit* (AIAA, 2008).

[17] W. J. Devenport, R. A. Burdisso, A. Borgoltz, P. A. Ravetta, M. F. Barone, K. A. Brown, and M. A. Morton, The Kevlar-walled anechoic wind tunnel, J. Sound Vib. **332**, 3971 (2013).

[18] See Supplemental Material at http://link.aps.org/supplemental/10.1103/PhysRevFluids.7.094401 for details of the boundary layer profile, spectrum results, spatial growth rate results, and bifurcations in Van der Pol oscillator to supplement the experimental data and analytical methods.

[19] S. Cho, J. Kim, and H. Choi, Control of flow around a low Reynolds number airfoil using longitudinal strips, Phys. Rev. Fluids **3**, 113901 (2018).

[20] S. Pröbsting and S. Yarusevych, Laminar separation bubble development on an airfoil emitting tonal noise, J. Fluid Mech. **780**, 167 (2015).

[21] S. Pröbsting, F. Scarano, and S. Morris, Regimes of tonal noise on an airfoil at moderate Reynolds number, J. Fluid Mech. **780**, 407 (2015).

[22] S. Lee, L. Ayton, F. Bertagnolio, S. Moreau, T. Chong, and P. Joseph, Turbulent boundary layer trailing-edge noise: Theory, computation, experiment, and application, Prog. Aerosp. Sci. **126**, 100737 (2021).

[23] T. Pyragienė and K. Pyragas, Delayed feedback control of forced self-sustained oscillations, Phys. Rev. E **72**, 026203 (2005).

[24] Z. B. Yang, Y. N. Wang, H. Zuo, X. W. Zhang, Y. Xie, and X. F. Chen, The Fourier spectral Poincaré map method for damage detection via single type of measurement, Measurement **113**, 22 (2018).